

Far Infrared Properties of M Dwarfs

Thomas. N. Gautier III ¹, G. H. Rieke ², John Stansberry ², Geoffrey C. Bryden ¹, Karl R. Stapelfeldt ¹, Michael W. Werner ¹, Charles A. Beichman ¹, Christine Chen ³, Kate Su ², David Trilling ², Brian M. Patten ⁴ and Thomas L. Roellig ⁵

ABSTRACT

We report the mid- and far-infrared properties of nearby M dwarfs. *Spitzer*/MIPS measurements were obtained for a sample of 62 stars at 24 μm , with subsamples of 41 and 20 stars observed at 70 μm and 160 μm respectively. We compare the results with current models of M star photospheres and look for indications of circumstellar dust in the form of significant deviations of K-[24 μm] colors and 70 μm / 24 μm flux ratios from the average M star values. At 24 μm , all 62 of the targets were detected; 70 μm detections were achieved for 20 targets in the subsample observed; and no detections were seen in the 160 μm subsample. No clear far-infrared excesses were detected in our sample. The average far infrared excess relative to the photospheric emission of the M stars is at least four times smaller than the similar average for a sample of solar-type stars. However, this limit allows the average fractional infrared luminosity in the M-star sample to be similar to that for more massive stars. We have also set low limits (10^{-4} to 10^{-9} M_{Earth} depending on location) for the maximum mass of dust possible around our stars.

Subject headings: Infrared: stars - stars: late-type - stars: fundamental parameters (colors) - planetary systems

¹Jet Propulsion Laboratory, California Institute of Technology, Pasadena, California 91109; Thomas.N.Gautier@jpl.nasa.gov

²Steward Observatory, University of Arizona, 933 North Cherry Avenue, Tucson, Arizona 85721

³National Optical Astronomy Observatories, Tucson, Arizona 85719

⁴Harvard-Smithsonian Center for Astrophysics, 60 Garden St., Cambridge, Massachusetts 02138

⁵NASA Ames Research Center, MS 245-6, Moffett Field, California 94035

1. Introduction

The study of dust around main sequence stars addresses intriguing questions in basic astrophysics while providing insights into the possible existence of planetary systems around these stars. The pioneering results from IRAS on infrared excess around stars like Vega (Aumann, et al. 1984) rapidly led to the realization that the circumstellar dust responsible for this emission could not survive for the lifetime of the star and that it must be replenished - from cometary or asteroid-type objects - just as the zodiacal cloud in our Solar System is replenished. The maintenance of this dust ultimately depends on collisions between asteroid-size objects, yielding fragments that collide with each other and eventually grind down to fine dust that is heated by the star and appears as an infrared excess. Thus the characteristics of circumstellar dust around a main sequence star (referred to hereafter as a “debris disk”) reflect the planet-building and planet-destroying processes occurring around that star.

The *Spitzer* Space Telescope (Werner, et al. 2004), building on the foundation established by IRAS and ISO, has already produced major advances in our understanding of the debris disk phenomenon. These include demonstration of the stochastic nature of debris disk evolution (Rieke, et al. 2005; Su, et al. 2006; Beichman, et al. 2005a), the first detection of debris disks around F, G, and K stars with known radial velocity companions (Beichman, et al. 2005b) and investigations of the frequency of occurrence of debris disks around solar type stars (Kim, et al. 2005; Bryden, et al. 2006). Here we present the results from a *Spitzer* search for dust associated with M dwarfs.

M dwarfs, with masses between 0.08 and 0.5 M_{\odot} , are the most common stars in the galactic plane. Thus the study of debris disks around them is needed to complete our understanding of the nature and incidence of debris disks in the solar neighborhood and the dependence of planet-forming processes on the mass of the central star. Since M stars are the most numerous stellar type, measurement of their debris disk frequency has large implications for the overall population of planetary systems in the galaxy. It may be that the nearest extrasolar planets to the Sun are orbiting M stars, a possibility that would be supported if M dwarfs frequently host debris systems.

However, the timescales and processes for dust expulsion may be considerably different for M stars than for their more luminous cousins (Plavchan, et al. 2005). Also, early results from precision radial velocity surveys have suggested that M stars have a lower frequency of giant planets than F and G stars (Butler, et al. 2004). It is important to determine if such a marked difference is also present in the relative frequency of debris disks between the M dwarfs and earlier types.

Finally, besides extending our understanding of the evolution of planetary systems by

investigating the frequency of debris disks around M dwarfs, these far-infrared measurements can determine basic parameters of the M stars themselves. We compare our data with current models of M dwarf photospheric emission and demonstrate how to refine determinations of M dwarf effective temperatures with the accurate $24\ \mu\text{m}$ data available with *Spitzer*.

2. New Observations

We observed 62, 41, and 20 M dwarfs, respectively, at 24, 70, and $160\ \mu\text{m}$, using the Multiband Imaging Photometer for *Spitzer* (MIPS; Rieke, et al. 2004). Our target stars are listed in Table 1. Stars of spectral type M7 and earlier (a total of 40), plus one M9 star, are part of a MIPS program to obtain photometry of all stars lying within 5 pc of the sun (*Spitzer* program ID 52). Twenty one later-type stars (M6 - M9) lying at distances of 6 to 18 pc were generally selected to be the brightest members of their spectral classes (*Spitzer* program ID 56). These later-type stars were observed only at $24\ \mu\text{m}$. While age determination of field M stars is notoriously difficult it is likely that the stars in our sample are nearly all older than 1 Gy.

The $24\ \mu\text{m}$ observations were made using the MIPS photometry observation template with the small dither size. For the nearby stars we generally used 1 cycle of the dither pattern (48s integration time). IL Aqr, LHS 3685 and LP 944-20 were exceptions receiving 180s, 136s and 1500s integration time respectively. This strategy typically resulted in very high signal-to-noise ratios (SNRs) at $24\ \mu\text{m}$. The more distant, later type, stars received from 1 to 9 dither cycles (48s to 1380s) at $24\ \mu\text{m}$; many of them were measured only to SNR ~ 10 .

The $70\ \mu\text{m}$ observations were also made using the MIPS photometry observation template with the small dither size and the default image scale (Rieke, et al. 2004). In this band, the required integration times were much longer than at $24\ \mu\text{m}$ and therefore automatically resulted in several cycles of the dither pattern. We limited the maximum integration time at $70\ \mu\text{m}$ to ~ 1000 seconds, both to fit the program within its time allocation and because the noise behavior of MIPS at longer integration times was unknown at the time these observations were scheduled (before the launch of *Spitzer*). Our goal of SNR ~ 6 on the photosphere was reached for many of the $70\ \mu\text{m}$ observations but the limitation on integration time resulted in low SNR detections or upper limits at $70\ \mu\text{m}$ for the fainter members of the sample.

To explore the possibility that these low-luminosity stars might possess very cold debris disks, $160\ \mu\text{m}$ photometry was carried out for 20 stars in the sample. Detection of the stellar

photospheres, whose median flux densities are expected to be a few mJy, was not achievable given *Spitzer's* measured extragalactic confusion limit of 8 mJy, 1σ (Dole, et al. 2004). The observations were therefore designed only to detect a source 3-5 times the confusion noise level. Four cycles of 160 μm photometry, totaling 84 sec of exposure time for each source, were used.

The data were processed using the MIPS instrument team Data Analysis Tool (DAT, version 2.73) described by Gordon, et al. (2005). For the 24 μm data, basic processing included slope fitting, flat-fielding, and corrections for droop and “jailbar” artifacts (DC offsets between adjacent detector columns that appear in measurements of bright sources). Further details are given by Engelbracht, et al. (2007). The 70 μm data processing also used the DAT, but was similar to that of the *Spitzer* pipeline version S12. Details are given in Gordon, et al. (2004). Mosaics were constructed using pixels interpolated to about 1/2 the native pixel scale of the arrays.

Fluxes were measured using fairly small apertures to improve the signal-to-noise ratios of the measurements, particularly given the relatively high spatial variability of the sky background at 70 μm . Most targets were measured using apertures 9.96" and 39.4" in diameter at 24 and 70 μm . The observed PSF full width at half maximum is 6.4" and 19.3", at 24 and 70 μm respectively. In a few cases nearby sources contributed significant flux at the target location, so we used apertures 25% smaller than those just described to reduce contamination. In one case (LHS 58 & 59, identified in the notes to Table 1), we deblended two sources at 70 μm using the model PSFs. The $\sim 10''$ aperture at 24 μm corresponds to disk radii of 7-90 AU at the various distances of our stars. At 70 μm , where only stars within 5 pc were observed, the $\sim 40''$ aperture corresponds to disk radii of 36-200 AU.

After extraction, the measured fluxes were corrected to infinite aperture. Aperture corrections were computed using STinyTim model PSFs (Krist 2005) for a 3000 K blackbody source. The model PSFs were smoothed until they provided good agreement with observed stellar PSFs out through the first Airy maximum.

Targets were usually identified in the 24 μm images using their J2000 coordinates and proper motions from SIMBAD. In most instances the agreement between the predicted and observed position was excellent (see Notes to Table 1 for cases where there was a significant disagreement). However, many of our later M type stars are rather dim, even at 24 μm , and special care was needed to ensure that the correct object was measured among many others in these fields. We confirmed a number of identifications with IRAC 3.6 μm images from program 35 (Multiplicity and Infrared Colors of Nearby MLT Dwarfs, Patten, et al. (2006)). The 24 μm photometric aperture was centered on the photocenter of the target. We used the same procedure at 70 μm when the source was clearly detected and there were

no confusing sources nearby. In cases where the 70 μm centroid position disagreed by more than 5'' with the 24 μm position, we forced the 70 μm aperture to be centered at the 24 μm position.

The fluxes we report are based on conversion factors of 1.048 $\mu\text{Jy}/\text{arcsec}^2/(\text{DN}/\text{s})$ and 16.5 $\text{mJy}/\text{arcsec}^2/\text{U70}$ at 24 and 70 μm , respectively (U70 = MIPS 70 μm unit). Table 1 lists the observed fluxes, their formal 1σ uncertainties (not including systematic calibration uncertainties) and 3σ upper limits where no flux could be determined.

For most of the observed stars, the error in the 24 μm photometry is dominated by calibration uncertainty, which contributes systematic 24 μm errors at the level of $\sim 5\%$ (see e.g. Beichman, et al. 2005a). However, we do not depend on the absolute calibration of the measurements to identify debris disks. We are instead limited by the scatter in the predictions of photospheric flux density from shorter wavelengths (see Su, et al. 2006). Background contamination by galactic cirrus or by extragalactic confusion is of relatively little importance. Dim sources, however, are limited by photon noise and by flat fielding uncertainties created by latent dark images. The effective noise level for the dimmest sources is ~ 0.05 mJy. Except for the faintest sources, we can detect excesses down to $\sim 15\%$ above the photosphere in this band.

At 70 μm the flux error is a combination of calibration uncertainty and background noise. The variable sky background, a combination of galactic cirrus and extragalactic confusion, presents a noise floor that cannot be improved with increases in integration time. This confusion noise is reached with integrations of 100's to 1000's of seconds depending on the local level of galactic cirrus brightness (Bryden, et al. 2006). This variation of the sky background within each frame, when convolved with our chosen beam size, is listed as the 70 μm flux error in Table 1. On top of this background noise, we have included a 10% systematic error at 70 μm , consistent with the uncertainty found within photospheric measurements of FGK stars (Beichman, et al. 2005a; Bryden, et al. 2006). A thorough discussion of the uncertainties in the 70 μm data can be found in these papers and in Gordon, et al. (2004). Excesses of 30% above the predicted photosphere for bright stars at 70 μm should be readily detectable.

At 160 μm , the DAT was used to calibrate the data, and mosaic the images at a pixel scale of 8''/pixel (half the native scale). The data were flux-calibrated using the standard conversion factor of 42.6 $\text{MJy}/\text{sr}/\text{MIPS160}$, where MIPS160 are the instrumental units that result after the data are normalized by the stim flashes. The uncertainty on the absolute calibration is 12% (Stansberry, et al. 2007). The MIPS 160 μm array suffers from a near-IR spectral leak that produces a strong ghost image overlapping the true 160 μm image for sources with stellar temperatures and J magnitudes brighter than 5.5 (MIPS data handbook,

<http://ssc.spitzer.caltech.edu/mips/dh/>). Only four of our brightest stars have a possibility of being effected by this leak. One of these stars (LHS 70) is the single case where one of our targets was detected at $160\ \mu\text{m}$, the spectral leak was detected and not the true $160\ \mu\text{m}$ emission. This detection is ignored and we give 3σ upper limits on the $160\ \mu\text{m}$ fluxes for all observed targets.

In most cases these limits are estimated from the scatter of pixels falling within a sky annulus with radii of $64'' - 128''$, and normalized to an aperture radius of $24''$. In some cases we also estimated the sky noise by dropping multiple $24''$ apertures on the images (away from the source position), and using the scatter of the fluxes in those apertures instead. The limits are corrected for the finite aperture size using a correction factor of 2.37, derived from STiny Tim model PSFs (Krist 2005) fitted to observed PSFs (Stansberry, et al. 2007). The resulting 3σ upper limits are presented in Table 1. There is considerable variation in the sensitivity achieved, due to the effects of galactic cirrus emission. The median upper limit is 74 mJy, but the limits for individual stars range from 53 to 963 mJy.

3. Interpretation

Because the intrinsic mid- and far-infrared properties of M stars are not well known, we take the approach of using our photometry and existing K band photometry to compare the M stars among themselves to look for evidence of excess emission. Extrapolations from K_S to $[24]$ require an accurate understanding of the photospheric colors that we determine in Section 3.1. We find no convincing evidence for any $24\ \mu\text{m}$ excesses above the photospheric outputs. In section 3.2 we use the ratio of our measured $70\ \mu\text{m}$ flux to a $70\ \mu\text{m}$ flux predicted from our $24\ \mu\text{m}$ measurement as our diagnostic tool. Again, we find no convincing evidence for a $70\ \mu\text{m}$ excess at greater than the 3σ level. The $160\ \mu\text{m}$ upper limits are discussed in section 3.3. Finally, in sections 3.4 and 3.5, we compare the results on dust excesses around M stars with those obtained by previous *Spitzer* studies of main sequence stars in the solar neighborhood.

3.1. Photospheric colors and $24\ \mu\text{m}$ excess

3.1.1. Photospheric colors

Table 2 lists the K_S band magnitudes and the colors derived from the infrared photometry. The K_S band data were obtained mostly from the 2MASS catalog (Cutri, et al. 2003a) but in some cases K measurements were obtained from other sources and transformed to

2MASS K_S (see notes to Table 2).

We show a color-color plot of $K_S - [24]$ vs. $V - K_S$ in Figure 1. The V magnitudes were obtained from NStars (<http://nstars.nau.edu/>), where possible, with SIMBAD as a secondary source. Eleven of our 62 objects have no accurate V photometry available. The $K_S - [24]$ colors are greater than zero, reflecting the fact that the spectral energy distributions of M stars do not transition to the Rayleigh-Jeans regime until well beyond $2 \mu\text{m}$. They also become increasingly red with later spectral type, reflected by larger $V - K_S$. With its long wavelength baseline, the $V - K_S$ color should be monotonic in spectral type/effective temperature. This plot should therefore allow us to identify excess candidate stars as outliers toward red $K_S - [24]$ from the overall trend. In fact, there is one such object, V1581 Cyg B. However, the figure also shows significant scatter, substantially more than expected purely from the errors in V , K_S or $[24]$, suggesting that there are significant variations in $V - K_S$ outside a purely monotonic relationship.

3.1.2. Identification of Excesses Using IRFM for Stellar Temperatures

Although accurate photometry for the entire sample is available in the near infrared, the issues shown in Figure 1 cannot be addressed with these measurements because M dwarf spectral type is not a sufficiently strong monotonic function of infrared colors. To improve over color-color plots, we have used a modified form of the infrared flux method (Blackwell, et al. 1986, and references therein) to determine effective temperatures for the stars in the sample, designated T_{irfm} . We can then plot $K_S - [24]$ as a function of T_{irfm} rather than $V - K_S$.

The effective temperature can be expressed as:

$$10 \log (T_{irfm}) = 42.32 - 5 \log \left(9.43 \times 10^{15} \left(\frac{S_\nu(24)}{(\int S_\nu d\nu)^{1/4} \alpha(T) \beta(T)} \right)^{2/3} \right) - (m_K + BC_K),$$

where $\alpha(T)$ is a term of order unity that is the ratio of the Planck function to the Rayleigh Jeans approximation at $24 \mu\text{m}$, and $\beta(T)$ is another term of order unity ($\beta(T) = 0.76$ independent of temperature for these stars) that is the ratio of the flux received through the $24 \mu\text{m}$ filter to the bolometric flux from the star, divided by the similar ratio for a blackbody at the effective temperature of the star. For stars of type M6 and later, we take bolometric corrections from Golimowski, et al. (2004). For stars earlier than M6, we used

$$BC_K = 0.42 + 1.45 (I - K) - 0.20 (I - K)^2.$$

This expression is based on that given by Reid & Hawley (2000), but has been modified to join better to the expression of Golimowski, et al. (2004) at the M5.5 to M6 transition. Our derived values of T_{irfm} are listed in Table 2.

Figure 2 shows the trend of K_S -[24] color vs. T_{irfm} . The scatter in the observed colors at a fixed temperature is small, consistent with it arising purely from the measurement errors.

We have compared the colors of the low mass stars with synthetic colors generated from a grid of models to be published by Brott et al. (see Brott & Hauschildt 2005). These models represent dusty atmospheres and are termed the “GAIA grid” because they were calculated in support of planning for the GAIA mission. They incorporate advances in the models published by Allard, et al. (2001), through improvements in parameters such as opacities and mixing lengths. The theoretical spectra were convolved with the wavelength-dependent instrumental response for the 2MASS K_S filter and the MIPS 24 μ m filter. Similar convolutions were performed for a Kurucz model A-star spectrum, and the two were ratioed to obtain colors relative to A-star colors for the low mass stars.

The synthetic colors are also compared with the measured ones in Figure 2. The observations follow roughly the theoretical curve, although the observed colors are systematically up to 20% less red in the 2500 - 3500 K range. Among the contributors to this discrepancy could be the effects of dust in the atmospheres, which can modify the absorption feature strengths in the K-band as well as affect the radiation transfer and hence the emitted flux in the 24 μ m band. These new observations should help provide a basis for improvement of models.

Figure 2 also plots the positions of the stars using a conventional spectroscopic temperature calibration. We took spectral types from the NStars tabulation as of December 31, 2006 wherever possible. In the remaining cases, the types are from SIMBAD as of the same date. In the latter instances, we consulted the primary references to verify the tabulated values. We used a type of M7.5 for LP 044-162, where the SIMBAD classification of M6.5 does not agree with the M7.5 found in the literature (Gizis, et al. 2000; Cruz, et al. 2003). From M0 through M6, the temperature calibration is from Tokunaga (2000), while from M6.5 through M9.5, we have assumed a linear relation with a slope of 200K per stellar sub-type. This relation joins the stellar and brown dwarf temperatures smoothly and is consistent in approach with the temperature scales for L dwarfs (Burgasser, et al. 2002). Arrows indicate the shifts in effective temperature from these values to those determined through the IRFM in this work. If an object has a deficiency in flux at 24 μ m relative to the conventionally determined temperature, then the IRFM calculation will indicate a higher temperature; if the object has a higher flux, then the IRFM will return a lower one. It can be seen that

most of the shifts are toward *higher* temperatures.

If these stars had a combination of underestimated temperature plus an excess at $24\ \mu\text{m}$, then the corrected temperatures should show considerable scatter in the plot (because the bolometric corrections on which the plot depends are based on a broad range of wavelengths). Instead, these points come to a well determined relationship with only small scatter. Therefore, we look for excesses among the stars where the IRFM shifts the temperature *lower* than the conventional calibration. An example is V1581 Cyg A, the star with a spectroscopic temperature of 2940K, adjusted to 2756K by the IRFM. However, this star has a low mass companion V 1581 Cyg C that is not resolved in our beam. This companion is faint enough in the visible not to bias the spectrum significantly, but it can contribute significantly at $24\ \mu\text{m}$ (e.g., Dawson & de Robertis 2000). A satisfactory fit to the properties of V 1581 Cyg A/C is a M6 primary and L1 secondary. The predicted brightness difference between A and C is 3 magnitudes at R, while the predicted difference at [24] is only 0.8 magnitudes. The observed value is 3.3 magnitudes at V (red version of V with an effective wavelength of $0.583\ \mu\text{m}$; Henry, et al. (1999)); a difference of 0.8 magnitudes at [24] explains the behavior in the figure. Thus, the behavior in both bands is explained by the M6/L1 binary hypothesis. Although the excess in this case is not related to a debris disk, the temperature shift illustrates how a debris disk could be identified.

The second object where we derive a lower temperature is V 1581 Cyg B, the single star suggested to have an excess in the color-color plot in Figure 1. It is not known to have a companion, but our results suggest it would be worthwhile to look for one. The third strongest example, LHS 3814, is also a double that is unresolved in our beam at $24\ \mu\text{m}$ (we have plotted it at the temperature of the hotter member). The fourth strongest example, LP 944-20, is thought to be only ~ 300 Myr old, much younger than a typical object in the sample (Ribas 2003). Assuming it has lower surface gravity than the other members of the sample, the molecular bands in the $2\ \mu\text{m}$ window will be strengthened consistent with its color deviation. All of the remaining objects fall in the region where no infrared excess is indicated.

3.1.3. $24\ \mu\text{m}$ excesses

Any star with a $24\ \mu\text{m}$ excess should lie above the photospheric color locus in Figure 2 or be shifted downward in temperature with our IRFM estimates. Although one could hypothesize that V1581 Cyg B has a debris-disk excess, since $24\ \mu\text{m}$ excesses are very uncommon around FGK stars (Bryden, et al. 2006) and since we find no large excess at $70\ \mu\text{m}$, this possibility is unlikely, and we will not consider it further. We therefore interpret

Figure 2 to show that there are no debris-disk-associated excesses at 24 μm .

We have repeated our analysis with artificial excesses at 24 μm . An excess of 20% above the stellar photosphere results in a downward adjustment of the indicated stellar temperature by about 200 K. We can compare this value with the scatter in stellar colors. The thick solid line in Figure 2 can be fitted by

$$K_S - [24] = -0.2915 + \frac{1}{1.267 \times 10^{-4} T + (2.389 \times 10^{-4} T)^2 + (2.2 \times 10^{-4} T)^3}$$

A predicted 24 μm flux density (P_{24} in Table 2) was produced from this $K_S - [24]$ and the measured K_S . Then the ratio of the measured 24 μm flux density to P_{24} was formed for each star (F_{24}/P_{24} in Table 2). This ratio has a mean of 1.04 and a standard deviation of 0.04 over our sample of 55 stars with derived T_{irfm} . This standard deviation corresponds to about 100 K in temperature. Excepting the two cases discussed in the preceding section, all the stars in this sample either have spectroscopically determined temperatures lower than T_{irfm} , or in agreement with this temperature. Therefore, the limits on excesses are of the order of 20%, 2σ .

3.2. 70 μm Excesses

Thirteen of the 20 stars with detected 70 μm fluxes have high quality measurements (SNR > 4 and no interference from nearby objects or cirrus) that allow a good determination of 70 μm excess. We formed the ratio, given in Table 2 as F_{70}/P_{70} , of the measured 70 μm flux to a predicted 70 μm flux derived from a black body extrapolation of our measured 24 μm flux using T_{irfm} as the black body temperature. In Figure 3 we have plotted this ratio vs. T_{irfm} for these 13 stars. Objects with only photospheric emission appear at a value of one on this plot, while those with excess emission at 70 μm would appear at values above unity. None of the 13 stars shows a 70 μm excess larger than the 3σ uncertainty in its (F_{70}/P_{70}) ratio. A 70 μm excess of 100% of the photospheric emission should be apparent in any of these stars. This null result is just at an interesting level of significance (see section 3.5.1 for discussion).

We also looked for 70 μm excesses by comparing our 70 μm detections among themselves. Any star with an excess should appear out of family with the, presumed, majority of non-excess stars. A $\pm 3\sigma$ range for F_{70}/P_{70} of (0.59, 2.18) was obtained for the stars in Figure 3 by finding the mean and standard deviation of $\log(F_{70}/P_{70})$. None of the 13 stars in Figure 3 exceed this range, confirming the conclusion of the previous paragraph. Among all twenty 70

μm detections ($\text{SNR} \geq 3.0$) only AD Leo, YZ Cet and LHS 39 fall outside of $0.59 < F_{70}/P_{70} < 2.18$, the range indicating no significant excess. AD Leo is anomalously low and may indicate a problem with the measurement of this star. YZ Cet may be contaminated by a background galaxy and should not be considered as having an excess without confirmation. LHS 39 is tantalizingly high, indicating the possibility of a $70 \mu\text{m}$ excess, but its $70 \mu\text{m}$ detection is only barely at 3.0σ significance and additional uncertainties entering the F_{70}/P_{70} ratio result in too low a significance to claim an excess.

3.3. $160 \mu\text{m}$ Upper Limits

The $160 \mu\text{m}$ band is more sensitive to the emission from colder dust, though the constraints vary greatly from star to star depending on the quality of the $160 \mu\text{m}$ data. Lalande 21185 and V1216 Sgr represent the range of $160 \mu\text{m}$ limits within our data. We discuss the $160 \mu\text{m}$ upper limits along with the shorter wavelength measurements in the following section.

3.4. Fractional dust luminosities

Figure 4 illustrates the limits on dust luminosity derived from our flux measurements. The upper limits on the ratio of dust luminosity to star luminosity (L_d/L_*) are shown as a function of dust temperature for two stars, Lalande 21185 and V1216 Sgr, representing the range of limits obtained for stars detected at $70 \mu\text{m}$. For each dust temperature, we calculate the maximum blackbody emission that is consistent with the observed 3σ limits. Each of the curved segments in Figure 4 corresponds to an individual observation at a specific wavelength, with the temperatures that an observation is most sensitive to depending on that wavelength. The $70 \mu\text{m}$ observations are particularly useful for constraining the emission from dust with temperatures $\sim 50 - 100 \text{ K}$, for which fractional luminosities greater than $\sim 10^{-4}$ are generally excluded.

The constraints on L_d/L_* in Figure 4 can be translated into upper limits on dust mass, for an assumed dust size and orbital location. Assuming micron-size dust, the $160 \mu\text{m}$ upper limits correspond to dust mass limits of $\sim 10^{-6}$ to $10^{-4} M_{\text{Earth}}$ of 20 K dust at 50 AU . Observations with moderate S/N at $70 \mu\text{m}$ translate to a maximum of $\sim 10^{-7} M_{\text{Earth}}$ of 50 K dust at 5 AU , while $24 \mu\text{m}$ observations limit warm, 250 K dust to $\sim 10^{-9} M_{\text{Earth}}$ at 0.2 AU (again assuming micron-size dust in both cases).

While fractional dust luminosities similar to that of $\beta \text{ Pic}$ ($L_d/L_* = 3 \times 10^{-3}$) would

have been detected in all stars with their photospheres detected at $70 \mu\text{m}$, luminosities as low as that of Vega ($L_d/L_* \sim 2 \times 10^{-5}$) could only be detected around stars with optimal data such as Lalande 21185.

3.5. Comparison of M stars with F, G, and K Stars

3.5.1. Previous Work

Debris disk excesses in M stars have been elusive, partly because of the increase in detection difficulty with decreasing stellar luminosity (see Section 3.5.2). Song, et al. (2002) and Plavchan, et al. (2005) have searched for excesses from M stars from IRAS data complemented by ground based measurements. Both studies find no credible excesses around mature M stars, that is those not associated with known young clusters nor showing spectroscopic signs of youth. Our results confirm this conclusion, using the more sensitive and accurate *Spitzer* data. Using reprocessed IRAS data, Backman, et al. (1986), reported an infrared excess from Ross 128 at 60 and $100 \mu\text{m}$. This was not confirmed by subsequent processing in the IRAS Faint Source Survey, and is also contradicted by the *Spitzer*/MIPS results. The 0.12 Jy excess they reported at $60 \mu\text{m}$ is 8 times larger than our 3 sigma upper limit at $70 \mu\text{m}$, and is therefore confidently excluded by our data. Using *Spitzer* spectroscopy, Jura, et al. (2004) report no excess for Ross 128. This leaves no known example of a mature main sequence M dwarf known to possess a far-infrared excess.

It is interesting to compare the present results with similar studies of stars of other spectral types to see whether M star debris disks are less common than disks around earlier type stars. As a comparison sample, we have used both the study of F5-K5 main-sequence field stars discussed by Bryden, et al. (2006) and the similar set of stars studied by Kim, et al. (2005). We combine all the data without regard to whether they apply to single stars, binaries, or stars with radial velocity planets. There are 69 stars in Bryden et al. and 35 in Kim et al., for a total of 104. Of these stars, 12 have detected excesses. We need to add ~ 2 more detections to allow for the weighted contribution of the four stars with bright excesses detected by IRAS and not re-observed (see Bryden, et al. 2006). We find that $13 \pm 4\%$ of these stars have excesses greater than 100%. Only one of the 69 stars in Bryden, et al. (2006), HD 69830, shows evidence for a significant $24 \mu\text{m}$ photometric excess more than 15% above the photosphere. Kim, et al. (2005) included only stars with cold excesses, so we cannot derive an independent statistic in this regard. However, it is clear that $24 \mu\text{m}$ excesses are uncommon in solar type main sequence field stars. We find no convincing $24 \mu\text{m}$ excess in a sample of 56 M stars.

The current sample of 20 M dwarfs with 3σ or better $70\ \mu\text{m}$ detections is quite small for purposes of drawing confident statistical inferences of debris disk frequency. Binomial statistics indicate that our result of no disk detections in the 20 stars only allows us to derive an upper limit of 14%, with 2σ confidence, to the incidence of disks among M dwarfs within 5pc of the Sun. This upper limit is right at the measured incidence level for more massive stars. Our upper limit is also consistent with a value of 13% reported by Lestrade, et al. (2006) for 20 to 200 Myr old field M dwarfs. However, we note that our 5 pc sample is likely to contain a large fraction of stars older than 200 Myr and may not be directly comparable.

Song, et al. (2002) find that a number of extremely young M stars have detectable excesses (i.e., Hen 3-600 and AU Mic, both less than 15 Myr old). Low, et al. (2005) report sensitive *Spitzer* measurements in the young TW Hya association where, of the 24 stars observed, 5 have significant excess at $24\ \mu\text{m}$ and 6 have excess at $70\ \mu\text{m}$. Chen, et al. (2005) confirm the excess in AU Mic. Thus, excesses are not uncommon in late-type stars, including M-type ones, at an age of ~ 10 Myr. However, they virtually completely disappear in mature low-mass stars.

3.5.2. Approach for Quantitative Comparison

To expand on the results in the preceding section, we need to use an appropriate metric to characterize debris systems. We will adopt the $70\ \mu\text{m}$ fractional excess, $F_{\text{excess}}/F_{\text{photosphere}}$, where F_{excess} is the flux density of the infrared excess and $F_{\text{photosphere}}$ that of the star itself, both at $70\ \mu\text{m}$. We use the $70\ \mu\text{m}$ fractional excess as a proxy for the fractional luminosity, $L_{\text{IR}}/L_{\text{star}}$, because it should be representative of disk luminosity for objects with no excess at shorter wavelengths.

As stars become less luminous and of lower temperature, it becomes increasingly difficult to measure infrared excesses to a given limit in fractional luminosity. This issue can be understood by considering a set of stars with varying temperature. The total luminosity of these objects, and thus the dust luminosity, will vary as T^4R^2 (where R is the stellar radius), but their photospheric outputs in the far infrared will be in the Rayleigh-Jeans regime and will only go as TR^2 . Thus, for a given threshold for excess detection above the photosphere, the fractional luminosity threshold will go as T^{-3} .

3.5.3. Application to M Star Sample

To obtain a quantitative measure of the average level of excess in the M star sample, we proceed in a manner analogous to stacking, a technique often used to enhance the average signal to noise ratio with observations of a suite of similar sources. Our various M stars have different expected signal levels and, as a result, the measurements are of intrinsically differing ratios of signal to noise. Therefore, we stack by taking the weighted average of the measured excess ratios at $70\mu\text{m}$. We eliminate from this average all objects with a nominal $\text{SNR} < 4$. We adopt for the remaining sources a net error consisting of the statistical error indicated in Table 1, plus a systematic error of 6% to reflect the scatter in measurements of bright objects at $70\mu\text{m}$ with MIPS (e.g. Gordon, et al. 2005). The result is a weighted average excess ratio at $70\mu\text{m}$ of 1.02 ± 0.05 ; that is, on average, there is no excess from these stars. We place a 2σ upper limit of 1.12 to the average excess ratio, or 0.12 to the excess (relative to the photospheric emission). We also compute an average effective temperature for this sample as a weighted average of the individual stellar effective temperatures where the weights are those used for the excess ratios. The result is $T = 3555\text{ K}$.

As a comparison sample, we use the FGK stars in Bryden, et al. (2006). We add in the four additional stars listed by Bryden et al. but measured in other *Spitzer* programs at half weight, since Bryden et al. are reporting on about half of their sample. We also add in DY Eri and eta Cas from this program. The result is an average excess ratio of 1.37 ± 0.033 . The average temperature of this sample computed in the same way as for the M stars is 5763 K. If we scale the average excess for this sample as T^3 , we predict that the average for the M stars if they have the same fractional luminosity in infrared excess emission is 0.09, just within the upper limit from our observations of 0.12.

Another effect that might lead to more prominent debris excesses in M stars is the scaling of dust mass to produce a given excess level, as a function of stellar luminosity. For a given fractional luminosity upper limit at a given wavelength, the minimum mass limits derived from the M star observations reported here are lower than would be the corresponding limits from more luminous stars. The reason is that the fractional dust luminosity is proportional to the total solid angle subtended by the dust as viewed from the star and that the temperature of the dust increases with the star's luminosity but decreases with distance from the star. Thus, at a fixed dust temperature, an increase in stellar luminosity requires that the dust be more distant which, in turn, requires more dust to subtend enough solid angle to keep L_d/L_* constant. In the simple case of a single fixed grain size, the number of grains to achieve a certain fractional luminosity at a given temperature scales with the luminosity of the star. Thus the minimum dust mass associated with an M star with $\sim 0.01 L_\odot$ solar luminosities would be $\sim 1\%$ of the corresponding minimum mass associated with a solar mass star, again

assuming the same limit to the fractional luminosity at a given wavelength. For typical M stars in the present sample, therefore, it is not surprising to note that the limits on 24 μm excesses correspond to masses as low as 10^{-9} earth masses, while at 70 μm , the non-detections could imply masses below 10^{-7} earth masses. Similar *Spitzer*/MIPS surveys for IR excess around FGK stars (e.g. Bryden, et al. 2006) can detect dust with lower luminosity relative to the central star (L_{dust}/L_{star} as low as 5×10^{-6}), but are less sensitive in terms of overall dust mass. The corresponding limit for non-detections of 70 μm excess around FGK stars is $> 10^{-6} M_{Earth}$, an order of magnitude above that for M stars.

3.5.4. Discussion

The fractional luminosity is the appropriate metric if we assume that hypothetical debris disks would have the same covering fraction independent of stellar type, thus absorbing and reradiating in the far infrared an equivalent fraction of the stellar output. Although the fractional luminosity provides a reasonable first-order metric to compare excesses in different stellar populations, there are many other considerations. For example, one would expect that cool, low-mass stars might be less effective at heating circumstellar dust than hotter ones, even after allowing for the difference in luminosity. The degree to which this expectation is realized depends on the optical properties of the debris disk particles. They are likely to be relatively large grain aggregates, whose behavior may differ substantially from that of typical interstellar grains. The grain loss mechanisms - photon pressure, Poyting-Robertson drag, and corpuscular winds - are generally different in low mass stars than in high mass ones, and may cause significant differences in their disks (e.g., strong winds may destroy them quickly). Also, our study probes debris disks at 70 μm and hence at a temperature of about 50 K. The equilibrium distance from a star of luminosity L for material at a given temperature scales as the square root of L . Given the steep dependence of stellar luminosity on mass, we are probing distinctly different physical regions around the M stars in this sample than the regions probed in observations of solar-like stars.

4. Conclusions

We observed a sample of 62 M stars to search for debris disk dust and to study photospheric models. We demonstrate a modified infrared flux method to determine the effective temperatures of these stars, taking advantage of the high accuracy measurements available at 24 μm with *Spitzer*. Using these effective temperatures, the $K_S - [24]$ colors of the stars agree reasonably well with the theoretical models of Brott et al. (private communication).

None of the stars in our sample has a high-weight detection of a mid- or far-infrared excess. In particular, the sample lacks the occasional stars with large excess that typifies samples of more massive stars. We compute a weighted average of the observed excess ratios at $70\ \mu\text{m}$ as a metric to characterize the excesses in this and other samples of stars. We find that the average excess in the M stars is at least four times less than the average in a sample of FGK stars. This limit is just at the level for equal fractional infrared luminosity in the two samples. We have set low limits (10^{-4} to $10^{-9}\ M_{\text{Earth}}$ depending on location) for the maximum mass of dust possible around our stars.

This work is based, in part, on observations made with the *Spitzer* Space Telescope, which is operated by the Jet Propulsion Laboratory, California Institute of Technology under contract with NASA. Support for this work was provided by NASA through contract 1255094. This work also makes use of data products from the Two Micron All Sky Survey, which is a joint project of the University of Massachusetts and the Infrared Processing and Analysis Center/California Institute of Technology, funded by the National Aeronautics and Space Administration and the National Science Foundation. We would further like to thank Peter Hauschildt for supplying us with results from the latest GAIA model spectra of late type stars.

REFERENCES

- Allard, F., Hauschildt, P., Alexander, D. R., Tamanai, A., & Schweitzer, A. 2001, *ApJ*, 556, 357
- Aumann, H. H., et al. 1984, *ApJ*, 278, L23
- Backman, D. E., Gillett, F. C. & Low, F. J. 1986, *Advances in Space Research*, 6, 43.
- Beichman, C. A., et al. 2005a, *ApJ*, 626, 1061
- Beichman, C. A., et al. 2005b, *ApJ*, 622, 1160
- Bryden, G., et al. 2006, *ApJ*, 636, 1098
- Blackwell, et al. 1986, *MNRAS*, 221, 427
- Brott, I., & Hauschildt, P. H. 2005, “The Three-dimensional Universe with GAIA”, (ESA SP-576), ed. C. Turon, K. E. O’Flaherty, M. A. C. Perryman, p. 565.
- Burgasser, A. T., et al. 2002, *ApJ*, 564, 421

- Butler, R. P., et al. 2004, ApJ, 617, 580
- Chen, C., et al. 2005, ApJ, 634, 1372
- Cruz K. L., et al. 2003, AJ, 126, 2421
- Cutri, R. M., et al. 2003a, “The 2MASS All-Sky Catalog of Point Sources”, University of Massachusetts and Infrared Processing and Analysis Center (IPAC/California Institute of Technology); VizieR On-line Data Catalog: II/246
- Cutri, R. M., et al. 2003b. “The 2MASS All-Sky Data Release Explanatory Supplement: VI.4 2MASS Photometric System”, University of Massachusetts and Infrared Processing and Analysis Center (IPAC/California Institute of Technology)
- Dawson, P. C., and de Robertis, M. M. 2000, AJ, 120, 1532
- Dole, H. et al. 2004 ApJS, 154, 93
- Engelbracht, et al. 2007 PASP, in press
- Dullemond, C. P., & Dominik, C. 2005 A&A, 434, 971
- Gizis, J. E., et al. 2000 AJ, 120, 1085
- Goldreich, P., Lithwick, Y., & Sari, R. 2004, ApJ, 614, 497
- Golimowski, D. A., Leggett, S. K., Marley, M. S., Fan, X., Geballe, T. R., Knapp, G. R., Vrba, F. J. et al. 2004, AJ, 127, 3516
- Gordon, K. D., et al. 2004, Proc. SPIE, 5487, 177
- Gordon, K. D., et al. 2005, PASP, 117, 503
- Henry, T. J., et al. 1999, ApJ, 512, 864
- Johnson, H. M. 1983, ApJ, 273, 702
- Jura, M., et al. 2004, ApJS, 154, 453
- Kalas, P., Liu, M. C. & Matthews, B.C. 2004, Science, 303, 1990
- Kenyon, S. J., & Bromley, B. C. 2004, AJ, 127, 513
- Kim, J. S., et al. 2005, ApJ, 632, 659
- Krist, J. E. 2005, <http://ssc.spitzer.caltech.edu/archanaly/contributed/stinytim.tar.gz>

- Lang, K. R. 1991, *Astrophysical Data*, Springer-Verlag, New York
- Leinhardt, Z. M., & Richardson, D. C. 2005, *ApJ*, 625, 427
- Liu, M.C., Matthews, B.C., Williams, J. P., and Kalas, P. G. 2004, *ApJ*, 608, L526
- Lestrade, J. F., Wyatt, M. C., Bertoldi, F., Dent, W. R. F. & Menten, K. M. 2006, *A&A*, 460, 733
- Low, F. J., Smith, P. S., Werner, M. W., Chen, C., Krause, K., Jura, M., and Hines, D. C. 2005, *ApJ*, 631, 1170
- Mould, J. R. & Hyland, A. R. 1976, *ApJ*, 208, 399
- Patten, B. M., et al. 2006, *ApJ*, 651, 502
- Persson, S. E., Aaronson, M. & Frogel, J. A. 1977, *AJ*, 82, 729
- Plavchan, P., Jura, M. & Lipsey, S. J. 2005, *ApJ*, 631, 1161
- Reid, N. & Hawley, S. L. 2000, “New Light on Dark Stars,” (Springer: New York)
- Ribas, I. 2003, *A&A*, 400, 297
- Rieke, G. H., et al. 2004, *ApJS*, 154, 25
- Rieke, G. H., et al. 2005, *ApJ*, 620, 1010
- Song, I., Weinberger, A. J., Becklin, E. E., Zuckerman, B. & Chen, C. 2002, *AJ*, 124, 514
- Stansberry, J., et al. 2007, *PASP*, in press
- Su, K., et al. 2006, *ApJ*, 653, 675
- Tokunaga, A. T. 2000, in *Allen’s Astrophysical Quantities*, 4th edition, ed. A.N. Cox, Springer-Verlag, NY, p. 143
- Werner, M. W., et al. 2004, *ApJS*, 154, 1

Table 1. Observational Data

Name	Gliese	LHS	SpT ¹	F ₂₄ (mJy)	F ₇₀ (mJy)*	F ₁₆₀ (mJy,3 σ)
AX Mic	GJ 825	66	M0	504.00 \pm 0.57	61.8 \pm 3.8	<75
LHS 38	GJ 412 A	38	M1	123.94 \pm 0.21	15.8 \pm 3.9 ^a	<67
GX And	GJ 15 A	3	M1.5	249.45 \pm 0.29	27.2 \pm 2.2	<102
Kapteyn’s Star	GJ 191	29	M1.5	98.46 \pm 0.14	4.6 \pm 2.4 ^b	...
LHS 70	GJ 887	70	M1.5	436.96 \pm 0.43	47.3 \pm 3.9	<53
Lalande 21185	GJ 411	37	M2	481.55 \pm 0.40	43.0 \pm 3.5	<62
LHS 1	GJ 1	1	M3	159.13 \pm 0.28	16.2 \pm 3.2	...
AD Leo	GJ 388	5167	M3	151.62 \pm 0.20	8.4 \pm 2.3	...
V2306 Oph	GJ 628	419	M3	104.83 \pm 0.23	19.2 \pm 2.8	<154
LHS 449	GJ 674	449	M3	120.51 \pm 0.22	10.4 \pm 7.3 ^c	<963
LHS 450	GJ 687	450	M3	160.17 \pm 0.21	28.1 \pm 3.4	<83
LHS 58	GJ 725 A	58	M3	183 \pm 3	31.9 \pm 3.3 ^d	<73 ^d
LHS 3685	GJ 832	3685	M3	163.15 \pm 0.18	19.5 \pm 4.1	<57
LHS 3814	GJ 860 A	3814	M3	146.0 \pm 0.4	117 \pm 61 ^e	...
GQ And	GJ 15 B		M3.5	49.46 \pm 0.20	5.3 \pm 1.9 ^f	...
Luyten’s Star	GJ 273	33	M3.5	127.16 \pm 0.22	11.4 \pm 3.7	<71
LHS 59	GJ 725 B	59	M3.5	115 \pm 3	11.0 \pm 3.3 ^d	... ^d
V1216 Sgr	GJ 729	3414	M3.5	83.67 \pm 0.27	17.0 \pm 5.7 ^g	<318
IL Aqr	GJ 876 A	530	M3.5	108.27 \pm 0.16	9.2 \pm 2.2	<67
Ross 128	GJ 447	315	M4	66.32 \pm 0.24	7.5 \pm 5.0	<61
Barnard’s Star	GJ 699	57	M4	188.45 \pm 0.25	29.1 \pm 4.4	<141
YZ Cet	GJ 54.1	138	M4.5	33.69 \pm 0.19	9.0 \pm 2.0 ^h	...
TZ Ari	GJ 83.1	11	M4.5	27.71 \pm 0.21	ⁱ	...
DY Eri C	GJ 166 C	25	M4.5	49.05 \pm 0.14	4.0 \pm 2.0	...
V577 Mon A	GJ 234 A	1849	M4.5	77.97 \pm 0.20	12.2 \pm 1.9 ^j	<128
LHS 451	GJ 682	451	M4.5	62.15 \pm 0.23	^k	...
EZ Aqr	GJ 866 A	68	M5	78.73 \pm 0.19	-4.2 \pm 3.5	...
LHS 39	GJ 412 B	39	M5.5	9.89 \pm 0.16	10.1 \pm 3.4 ^l	...
FL Vir	GJ 473A	333	M5.5	49.4 \pm 0.4	3.0 \pm 2.0	...
Proxima Cen	GJ 551	49	M5.5	235.06 \pm 0.37	^m	...
Ross 248	GJ 905	549	M5.5	52.78 \pm 0.16	10.7 \pm 2.0 ⁿ	...
LHS 2	GJ 1002	2	M5.5	14.60 \pm 0.18	4.1 \pm 2.6	...
LHS 1565	GJ 1061	1565	M5.5	29.65 \pm 0.22	^p	<63
V1581 Cyg A	GJ 1245 A	3494	M5.5	27.0 \pm 1.6	-12 \pm 10 ^q	<387
LHS 1375	GJ 3146	1375	M5.5 s	3.31 \pm 0.13
LHS 288	GJ 3618	288	M5.5	10.71 \pm 0.14	^r	...
UV/BL Cet	GJ 65 B	10	M6	95.74 \pm 0.22 ^r	5.6 \pm 1.9 ^s	<68
GL 316.1	GL 316.1	2034	M6 s	1.35 \pm 0.11
Wolf 359	GJ 406	36	M6	49.90 \pm 0.30	^t	...
V1581 Cyg B	GJ 1245 B	3495	M6	18.0 \pm 0.7	-12 \pm 10 ^q	...
GJ 283B	GJ 283 B	234	M6.5 s	1.05 \pm 0.13
DX Cnc	GJ 1111	248	M6.5	17.18 \pm 0.22	6.0 \pm 3.0 ^u	<101
LHS 292	GJ 3622	292	M6.5	9.41 \pm 0.13	1.1 \pm 1.9 ^v	...
LHS 2930	GJ 3855	2930	M6.5 s	1.63 \pm 0.1
GJ 644C	GJ 644 C	429	M7	4.17 \pm 0.12
LHS 3003	GJ 3877	3003	M7	3.75 \pm 0.11

Table 1—Continued

Name	Gliese	LHS	SpT ¹	F ₂₄ (mJy)	F ₇₀ (mJy)*	F ₁₆₀ (mJy,3 σ)
2MASS J09522188-1924319			M7 s	0.53 \pm 0.07
2MASS J23062928-0502285			M7.5 s	1.35 \pm 0.12
LP 044-162			M7.5 ²	1.08 \pm 0.08
LP 349-025			M8 s	2.31 \pm 0.12
LP 326-021			M8 s	0.89 \pm 0.09
LP 412-031			M8 s	0.74 \pm 0.07
LP 771-021			M8 s	0.41 \pm 0.05
LHS 2397 A	GJ 3655	2397A	M8 s	0.99 \pm 0.06
ESO 207-61			M8 s	0.16 \pm 0.04
TVLM 513-46546			M8.5 s	1.03 \pm 0.1
LP 944-20	...		M9 s	3.95 \pm 0.05	7 \pm 3 ^w	...
LHS 2065	GJ 3517	2065	M9	1.9 \pm 0.09
TVLM 868-110639			M9 s	0.68 \pm 0.03
BRI 0021-0214			M9.5 s	1.26 \pm 0.05
2MASSW J1733189+463359			M9.5 s	0.28 \pm 0.03
DENIS-P J0021.0-4244			M9.5 s	0.26 \pm 0.04

*Entries with an ellipsis (...) in the 70 μ m column are from *Spitzer* program 56.

¹Spectral types are from the NStars data base except for those marked “s” which are from Simbad.

²See text for LP 044-162 spectral type source.

^aLHS 38: Some cirrus at 70 μ m

^bKapteyn’s: No source apparent at 70 μ m. Photometry at reference position.

^cLHS 449: Bad cirrus confusion at 70 μ m

^dLHS 58 & 59: 14'' separation. 70 μ m fluxes from deblending. 160 μ m upper limit is for the combination.

^eLHS 3814: Bad cirrus, especially at 70 μ m

^fGQ And: 35'' separation from GX And: possible slight blending at 70 μ m.

^gV1216 Sgr: Bad Cirrus at 70 μ m

^hYZ Cet: Diffuse source, probable background contamination

ⁱTZ Ari: Bright background source 20'' north accounts for flux

^jV577 Mon A: 2'' separation from GJ23B. Photometry includes both sources in both bands

^kLHS 451: Bad cirrus confusion: no source apparent at 70 μ m

^lLHS 39: 70 μ m photometry done at 24 μ m position. 32'' separation from LHS 38

^mProxima Cen: Very bad cirrus at 70 μ m.

ⁿRoss 248: 70 μ m source offset slightly from 24 μ m source; possible contamination.

^pLHS 1565: Bright background galaxy. No 70 μ m photometry possible

^qV1581 Cyg A & B: 8'' separation and bad cirrus. 70 μ m photometry includes both sources

^rLHS 288: Not on the 70 μ m image (error in requested pointing)

^sUV Cet/BL Cet: 2'' separation. Photometry is for both sources in both bands

^tWolf 359: Not on the 70 μm image (error in requested pointing)

^uDX Cnc: No source apparent at 70 μm . Photometry at reference position.

^vLHS 292: 70 μm photometry at 24 μm position. Nearby 70 μm source.

^wLP 944-20: Faint source at 70 μm ; another 70 μm source 50'' north

Table 2. Colors and Derived Quantities

Name	Dist(pc)	SpT	T_{eff}	T_{irfm}	B.C.	K_S^*	$K_S-[24]^\dagger$	P_{24}^\ddagger	F_{24}/P_{24}^\ddagger	P_{70}^\ddagger	F_{70}/P_{70}^\ddagger
AX Mic	3.95	M0	3800	3987	2.370	3.07 ± 0.02^a	0.19 ± 0.06	502.04	1.00	58.37	1.06
LHS 38	4.85	M1	3680	3591	2.530	4.77 ± 0.02	0.37 ± 0.06	116.58	1.06	14.44	1.09
GX And	3.56	M1.5	3605	3646	2.470	4.02 ± 0.02	0.38 ± 0.06	228.78	1.09	29.03	0.94
Kapteyn's Star	3.92	M1.5	3605	3554	2.474	5.05 ± 0.02	0.40 ± 0.06	88.49	1.11 ^d	11.46	$< 0.6^d$
LHS 70	3.29	M1.5	3605	3636	2.530	3.36 ± 0.02^a	0.33 ± 0.06	421.41	1.04	50.86	0.93
Lalande 21185	2.54	M2	3530	3469	2.530	3.35 ± 0.02^b	0.42 ± 0.06	432.61	1.11 ^d	56.10	0.77 ^d
LHS 1	4.36	M3	3380	3563	2.530	4.52 ± 0.2	0.39 ± 0.21	148.05	1.07	18.55	0.87
AD Leo	4.89	M3	3380	3360	2.648	4.59 ± 0.02	0.41 ± 0.06	148.76	1.02	17.73	0.47
V2306 Oph	4.24	M3	3380	3265	2.710	5.08 ± 0.02	0.49 ± 0.06	99.15	1.06	12.28	1.56
LHS 449	4.54	M3	3380	3471	2.580	4.86 ± 0.02	0.42 ± 0.06	112.58	1.07	14.07	< 1.6
LHS 450	4.54	M3	3380	3332	2.710	4.55 ± 0.02	0.43 ± 0.06	155.96	1.03	18.74	1.50
LHS 58	3.53	M3	3380	3369	2.650	4.43 ± 0.02	0.45 ± 0.06	171.81	1.07	21.40	1.49
LHS 3685	4.93	M3	3380	3657	2.470	4.47 ± 0.02^c	0.37 ± 0.06	150.66	1.08	18.98	1.03
LHS 3814	4.03	M3	3380	3211	2.648	4.78 ± 0.03	0.56 ± 0.06	132.40	1.10	17.13	< 10.7
GQ And	3.56	M3.5	3280	3157	2.708	5.95 ± 0.02	0.55 ± 0.06	46.12	1.07	5.81	< 1.0
Luyten's Star	3.79	M3.5	3280	3273	2.710	4.86 ± 0.02	0.49 ± 0.06	119.93	1.06	14.90	0.77
LHS 59	3.53	M3.5	3280	3239	2.710	5.00 ± 0.02	0.52 ± 0.06	106.87	1.08	13.48	0.82
V1216 Sgr	2.97	M3.5	3280	3215	2.710	5.37 ± 0.02	0.54 ± 0.06	76.76	1.09	9.81	< 1.8
IL Aqr	4.70	M3.5	3280	3240	2.760	5.01 ± 0.02	0.46 ± 0.06	105.85	1.02	12.69	0.72
Ross 128	3.35	M4	3180	3130	2.760	5.65 ± 0.02	0.57 ± 0.06	61.53	1.08	7.79	< 1.9
Barnard's Star	1.83	M4	3180	3039	2.850	4.52 ± 0.02	0.57 ± 0.06	181.72	1.04	22.19	1.31
YZ Cet	3.72	M4.5	3105	3052	2.810	6.42 ± 0.02	0.60 ± 0.06	31.38	1.07	3.97	2.27
TZ Ari	4.45	M4.5	3105	2995	2.810	6.65 ± 0.02	0.62 ± 0.06	26.11	1.06	3.27	...
DY Eri C	5.03	M4.5	3105	3058	2.810	5.96 ± 0.02	0.55 ± 0.06	47.80	1.03	5.77	< 1.0
V577 Mon A	4.09	M4.5	3105	3074	2.810	5.49 ± 0.02	0.59 ± 0.06	73.14	1.07	9.17	1.33
LHS 451	5.01	M4.5	3105	3302	2.710	5.61 ± 0.02	0.46 ± 0.06	59.43	1.05	7.28	...
EZ Aqr	3.45	M5	3030	2855	2.943	5.54 ± 0.02	0.65 ± 0.06	78.21	1.01	9.31	< 1.1
LHS 39	4.85	M5.5	2940	2811	2.943	7.84 ± 0.03	0.69 ± 0.06	9.65	1.03	1.17	< 9.0
FL Vir	4.39	M5.5	2940	2866	2.943	6.04 ± 0.02	0.63 ± 0.06	49.04	1.00	5.80	< 1.0
Proxima Cen	1.30	M5.5	2940	2855	2.943	4.35 ± 0.02^a	0.64 ± 0.06	234.04	1.00	27.80	...
Ross 248	3.16	M5.5	2940	2928	2.940	5.93 ± 0.02	0.60 ± 0.06	52.46	1.01	6.23	1.72
LHS 2	4.69	M5.5	2940	2792	2.943	7.44 ± 0.02	0.72 ± 0.06	14.10	1.04	1.73	< 4.5
LHS 1565	3.69	M5.5	2940	2879	2.940	6.61 ± 0.02	0.66 ± 0.06	28.80	1.03	3.50	...
V1581 Cyg A	4.54	M5.5	2940	2756	2.940	6.85 ± 0.02	0.79 ± 0.08	24.82	1.09	3.20	< 10.3
LHS 1375	8.50	M5.5	2940	2821	3.034	8.98 ± 0.05	0.65 ± 0.09	3.36	0.99		

Table 2—Continued

Name	Dist(pc)	SpT	T_{eff}	T_{irfm}	B.C.	K_S^*	K_S -[24] [†]	P_{24}^\ddagger	F_{24}/P_{24}^\ddagger	P_{70}^\ddagger	F_{70}/P_{70}^\ddagger
LHS 288	4.49	M5.5	2940	2832	2.943	7.73 ± 0.03	0.67 ± 0.06	10.54	1.02	1.27	...
UV/BL Cet	2.68	M6	2850	2874	2.940	5.34 ± 0.02	0.66 ± 0.06	93.03	1.03	11.32	< 0.5
GL 316.1	14.06	M6	2850	2724	3.034	10.05 ± 0.05	0.74 ± 0.12	1.33	1.02		
Wolf 359	2.39	M6	2850	2857	2.943	6.08 ± 0.02	0.69 ± 0.06	47.51	1.05
V1581 Cyg B	4.54	M6	2850	2602	3.030	7.39 ± 0.02	0.88 ± 0.07	16.89	1.07	2.14	< 15.4
GJ 283B	8.90	M6.5	2750	^e	...	9.26 ± 0.05	-0.32 ± 0.15	2.48	0.42 ^e		
DX Cnc	3.63	M6.5	2750	2746	3.030	7.26 ± 0.02	0.71 ± 0.06	17.12	1.00	2.04	< 4.4
LHS 292	4.54	M6.5	2750	2675	3.069	7.93 ± 0.03	0.73 ± 0.06	9.67	0.97	1.12	< 5.1
LHS 2930	9.63	M6.5	2750	2711	3.069	9.79 ± 0.05	0.69 ± 0.10	1.70	0.96		
GJ 644C	6.45	M7	2650	2700	3.060	8.82 ± 0.05	0.74 ± 0.08	4.19	0.99		
LHS 3003	6.40	M7	2650	2704	3.060	8.93 ± 0.05	0.73 ± 0.08	3.78	0.99		
2MASS J0952-1924	...	M7	2650	^e	...	10.87 ± 0.05	0.55 ± 0.16	0.67	0.79 ^e		
2MASS J2306-0502	...	M7.5	2550	2479	3.070	10.30 ± 0.05	0.99 ± 0.12	1.26	1.07		
LP 044-162	12.5	M7.5	2750	2589	3.070	10.40 ± 0.05	0.85 ± 0.11	1.06	1.02		
LP 349-025	7.8	M8	2450	2570	3.100	9.57 ± 0.05	0.84 ± 0.09	2.30	1.00		
LP 326-021	...	M8	2450	2559	3.100	10.62 ± 0.05	0.86 ± 0.13	0.88	1.01		
LP 412-031	14.64	M8	2450	2728	3.056	10.64 ± 0.05	0.68 ± 0.13	0.77	0.96		
LP 771-021	16.23	M8	2450	2591	3.100	11.42 ± 0.05	0.82 ± 0.15	0.41	0.99		
LHS 2397 A	14.29	M8	2450	2380	3.100	10.74 ± 0.05	1.09 ± 0.10	0.92	1.08		
ESO 207-61	18.48	M8	2450	^e	...	12.11 ± 0.05	0.49 ± 0.28	0.25	0.65 ^e		
TVLM 513-46546	9.82	M8.5	2350	2404	3.120	10.71 ± 0.05	1.11 ± 0.13	0.92	1.12		
LP 944-20	4.97	M9	2250	2123	3.150	9.55 ± 0.02	1.41 ± 0.06	3.58	1.10	0.48	< 18.8
LHS 2065	8.53	M9	2250	2420	3.150	9.94 ± 0.05	1.00 ± 0.09	1.85	1.03		
TVLM 868-110639	17.39	M9	2250	2193	3.150	11.35 ± 0.05	1.30 ± 0.09	0.63	1.08		
BRI 0021-0214	12.12	M9.5	2150	2284	3.180	10.54 ± 0.05	1.16 ± 0.08	1.21	1.04		
2MASSW J1733+4633	...	M9.5	2150	2512	3.180	11.89 ± 0.05	0.87 ± 0.14	0.28	0.99		
DENIS-P J0021.0-4244	...	M9.5	2150	^d	...	12.30 ± 0.05	1.20 ± 0.18	0.22	1.21 ^d		

* K_S is the 2MASS magnitude. K magnitudes footnoted ^a, ^b and ^c were converted to K_S using the 2MASS-CIT transformation in Cutri, et al. (2003b)

[†]24um zero point magnitude taken as 7.14 Jy.

[‡]Predicted values of the flux at 24 and 70 μ m, P_{24} and P_{70} are derived as described in the text, except that footnoted values use T_{eff} instead of T_{irfm} . Upper limits are at the 2 σ level.

^aPhotometry from Mould, J.R. & Hyland, A.R., 1976, ApJ, 308, 399

^bPhotometry from Persson et al., 1977, AJ, 82, 9

^cPhotometry from Leggett, S.K. 1992, ApJS, 82, 351

^dExcluded from K_S -[24] calculation due to low SNR, but fits the trend.

^eExcluded from K_S -[24] calculation due to low SNR, and is highly discrepant.

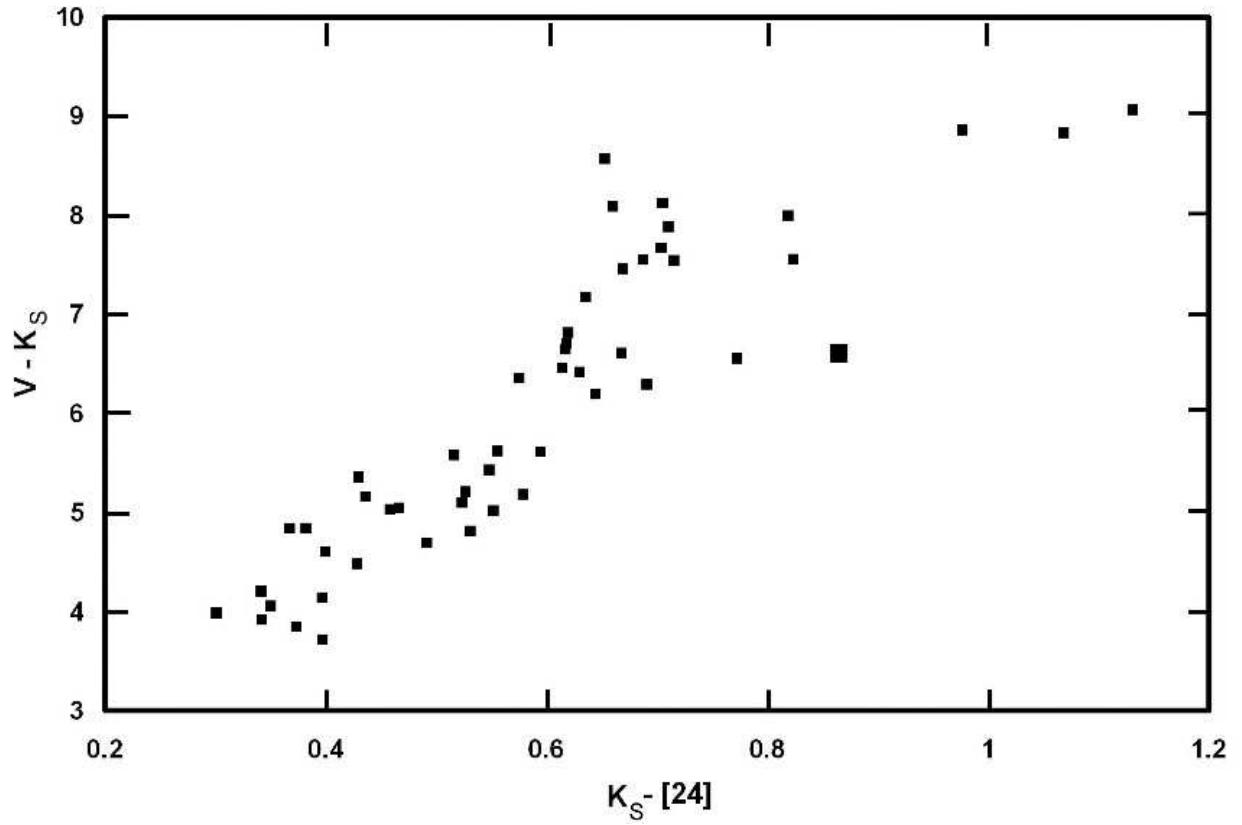


Fig. 1.— $K_S - [24]$ colors vs. $V - K_S$. The large symbol is for V1581 Cyg B, the only object with a possible excess at $24\mu\text{m}$ identified through this test.

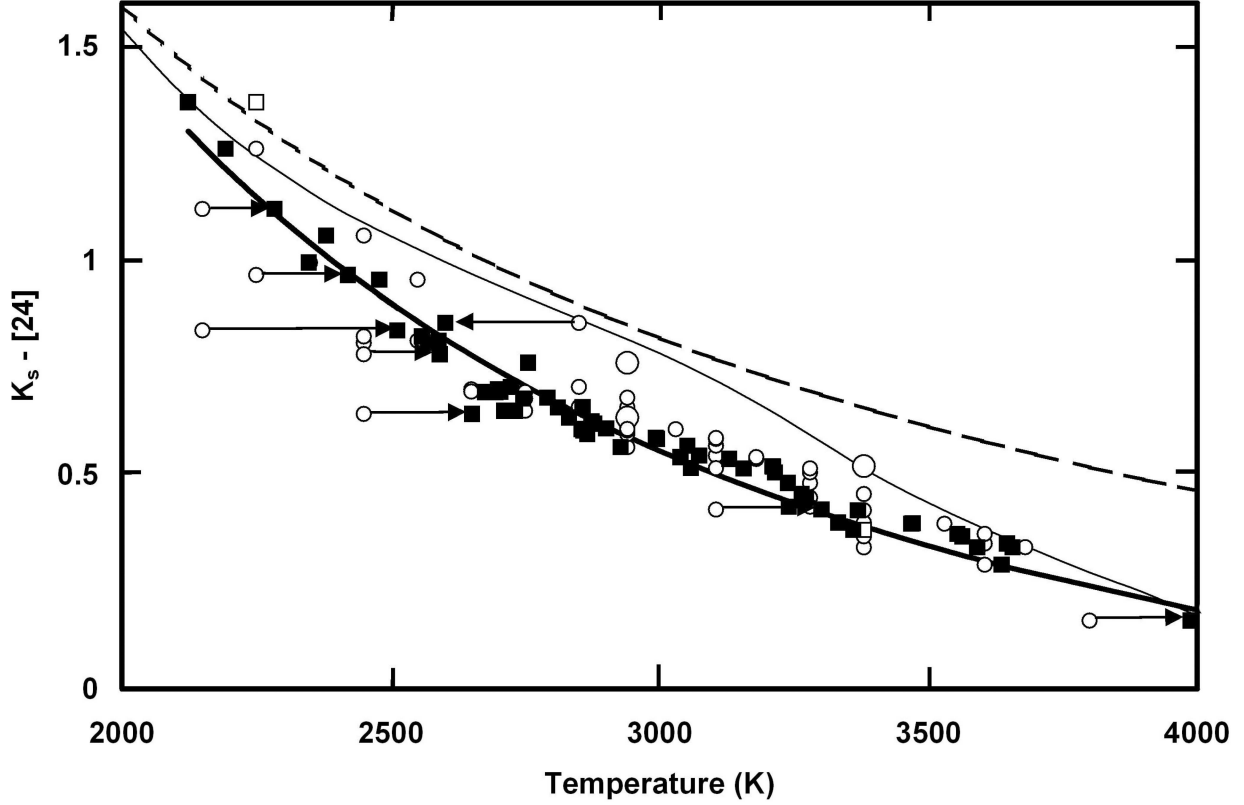


Fig. 2.— $K_S-[24]$ colors vs. T_{eff} and T_{irfm} . The open circles show T_{eff} from the spectral type, while the filled boxes are the result of deriving T_{irfm} from the infrared flux method, as described in the text. Unresolved binaries are indicated by larger circles and young objects by open squares. Cases with large unexplained differences are connected with arrows from the spectral estimate to the infrared flux method one. The thin solid line shows the prediction from the atmospheric models of Brott & Hauschildt (2005). The thick solid line is the fit to $K_S-[24]$ vs. T_{irfm} derived in this paper. The dashed line shows the color of a black body.

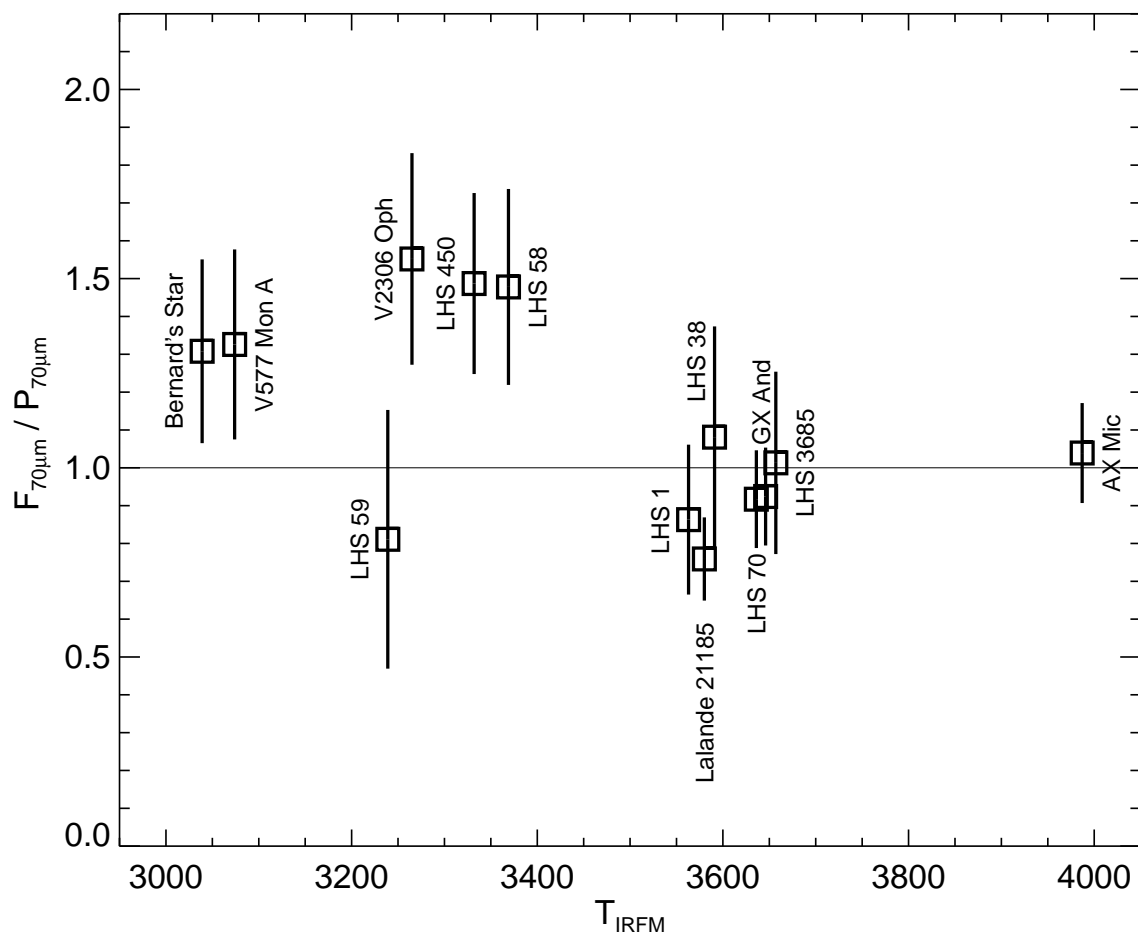


Fig. 3.— The ratio of measured to predicted $70\mu\text{m}$ flux vs. the effective temperature of the sources determined from the infrared flux method. Only sources that were unambiguously detected at $70\mu\text{m}$ are included (i.e. $\text{SNR} > 3$ and no obvious indications of contamination from background sources; see notes to Table 2). The $70\mu\text{m}$ prediction is extrapolated from the measured $24\mu\text{m}$ flux using a black body at T_{irfm} for each star, as described in the text.

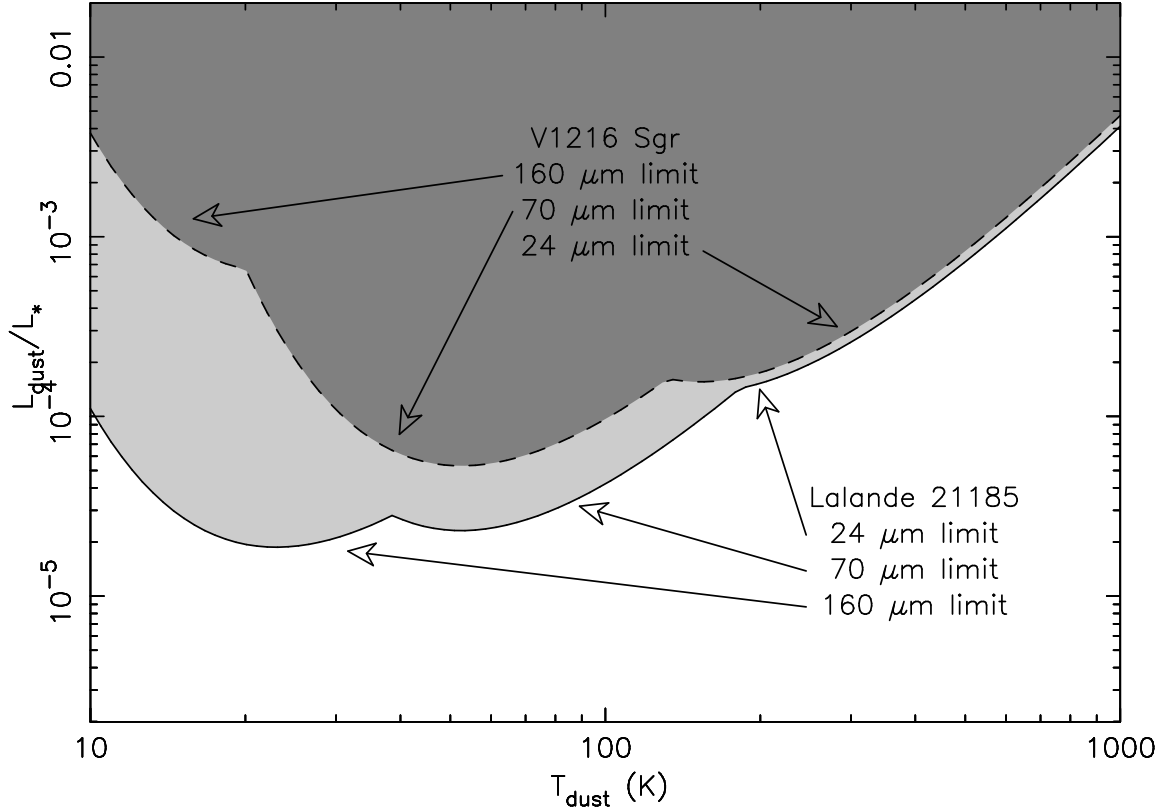


Fig. 4.— Detection limits for circumstellar dust. The MIPS detection levels are shown for two stars as a function of dust luminosity and temperature. The light grey region is ruled out by the detection upper limits for Lalande 21185 (solid line), a relatively bright star with a clean $160 \mu\text{m}$ image, while the dark grey region is ruled out for V1216 Sgr (limits shown as a dotted line), a star located in a very noisy $160 \mu\text{m}$ field. Both stars have 1σ errors of $\sim 5\%$ at $24 \mu\text{m}$, but their relative accuracies diverge at longer wavelengths; 1σ errors at $160 \mu\text{m}$ are 0.9 and 70 times the stellar photosphere for Lalande 21185 and V1216 Sgr respectively. In both cases, 3σ limits are plotted.